Electronic supplementary information (ESI)

Bio-Inspired Design of Self-Supported Bismuth Microforest for High Performance Sodium Storage

Jia Bai[a], Yan Liu[a,*], Ben Pu[a], Qi Tang[a], Yongbin Wang[a], Ruihan Yuan[b], Jin Cui[a], Yi Yang[a], Xiaojia Zheng[b], Bin Zhou[b,*] and Weiqing Yang[a,c,*]

[a] Key Laboratory of Advanced Technologies of Materials (Ministry of Education), School of Materials Science and Engineering, Southwest Jiaotong University, Chengdu, 610031, PR China.

[b] Sichuan Research Center of New Materials, Institute of Chemical Materials, China Academy of Engineering Physics, Chengdu, 610200, PR China.

[c] Research Institute of Frontier Science, Southwest Jiaotong University, Chengdu, 610031, PR China.

* Corresponding authors: y_liu@swjtu.edu.cn, bzhou@caep.cn, wqyang@swjtu.edu.cn.

Chemicals. Bismuth nitrate pentahydrate ($Bi(NO_3)_3 \cdot 5H_2O$, 99%) and acetonitrile (99%) were obtained from Aladdin Co., Ltd. Nitric acid (HNO_3, 65%~68%), hydrochloric acid (HCl, 36%~38%), acetone (99%), and anhydrous ethanol were purchased from Chengdu Kelong Chemicals Co., Ltd. Porous copper foil (99.9%) was acquired from Kejing Technology Co., Ltd. All chemicals were directly used as supplied without any purification. All aqueous solutions were prepared with deionized water.

Finite-element analysis. Finite-element method is a powerful numerical method used to analyze and solve complex engineering problems by using a limited number of unknowns to approximate an infinitely unknown real system constantly. To simulate the Na^+ concentration gradient and stress distribution in different geometrical structures

(rectangle, triangle and tree-like shape with the same height and bottom length) during sodiation process, a 2D multi-physical coupled model similar to that of Yu et al.[1] was constructed and solved by COMSOL Multiphysics software. Briefly, the diffusion of sodium ions in materials follows Fick's law of diffusion and the effect of convection is neglected. The governing equation for the transport process of sodium ions in the electrode solid phase is as follow:

$$\frac{\partial c}{\partial \mathrm{t}} = \nabla \cdot (D \nabla c) \tag{1}$$

where, c stands for the concentration of sodium ions in the materials; D is the sodium ion diffusion coefficient; t is the reaction time. As for boundary conditions, the bottom side faces of three different shapes serve as impermeable boundaries, while the sodium ion concentration of the rest of side faces is set to constant. The material is subject only to elastic deformation during the simulation and the strain induced by the diffusion is set linear to the sodium ion concentration. The material's linear elastic deformation process can be described by:

$$\nabla \cdot (C : \varepsilon_{\mathrm{e}}) = 0 \tag{2}$$

$$\varepsilon_{\mathrm{e}} = \varepsilon - \varepsilon_{\mathrm{i}} \tag{3}$$

$$\varepsilon_{\mathrm{i}} = \beta_{\mathrm{h}} M (c - c_{\mathrm{r}}) \tag{4}$$

$$\varepsilon = \frac{1}{2}[(\nabla L)^T + \nabla L] \tag{5}$$

where C stands for the fourth-order elastic tensor and is a function (C=C(E, v)) of Young's modulus (E) and Poisson's ratio (v); ε_{e}, ε, and ε_{i} are the elastic strain, total strain force, and inelastic strain, respectively; c_{r} is the reference sodium ion concentration; β_{h} is the adsorption expansion coefficient; M is the molar mass; L is the displacement. The bottom side faces of three different shapes are subjected to fixed constraint boundary conditions, while the remaining side faces are assigned free deformation boundary conditions.

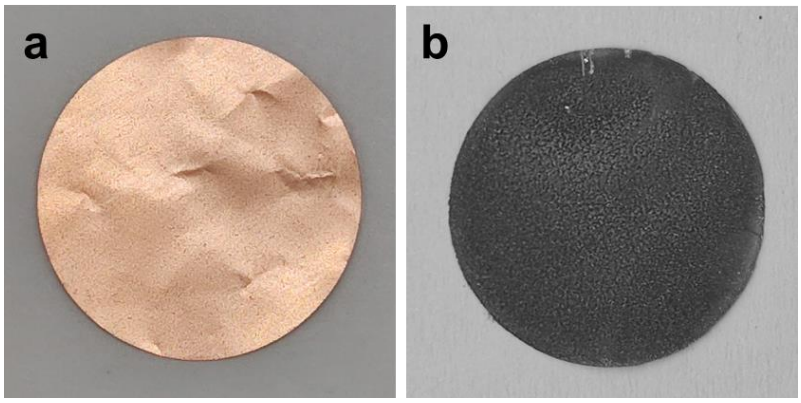

Fig. S1 Photographs of (a) porous Cu foil and (b) Bi MF.

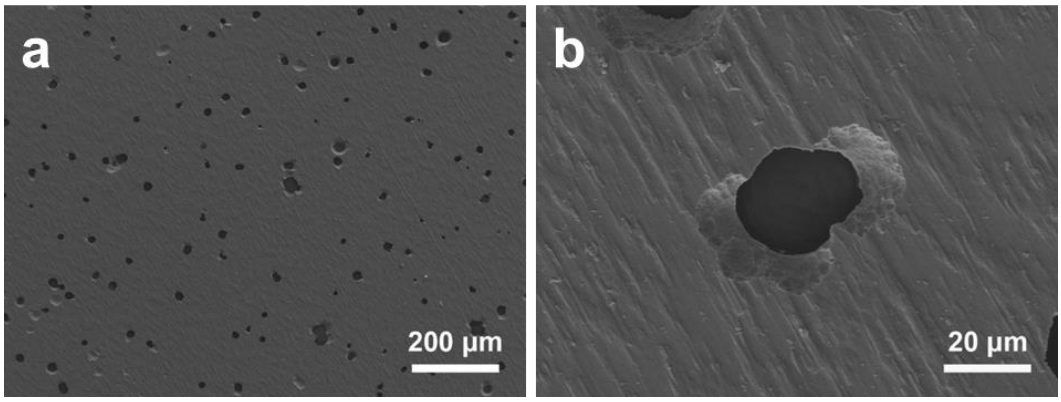

Fig. S2 (a, b) SEM images of porous Cu foil.

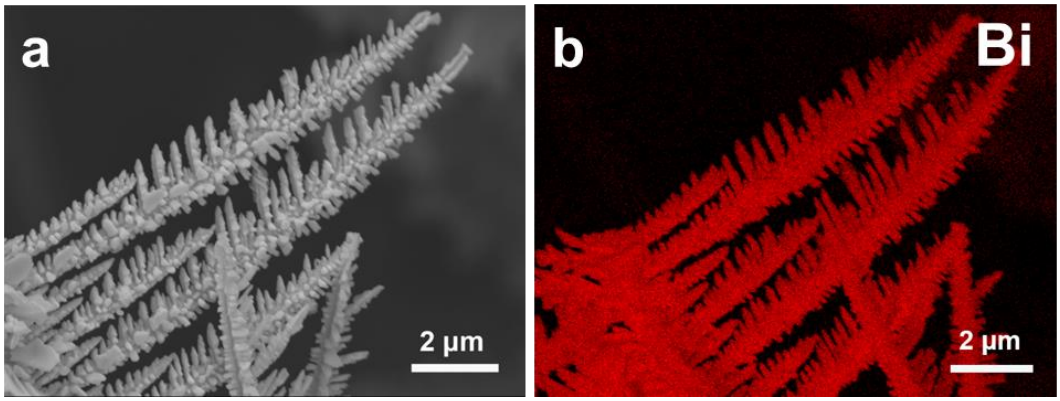

Fig. S3 (a) SEM image, (b) EDS image of Bi MF.

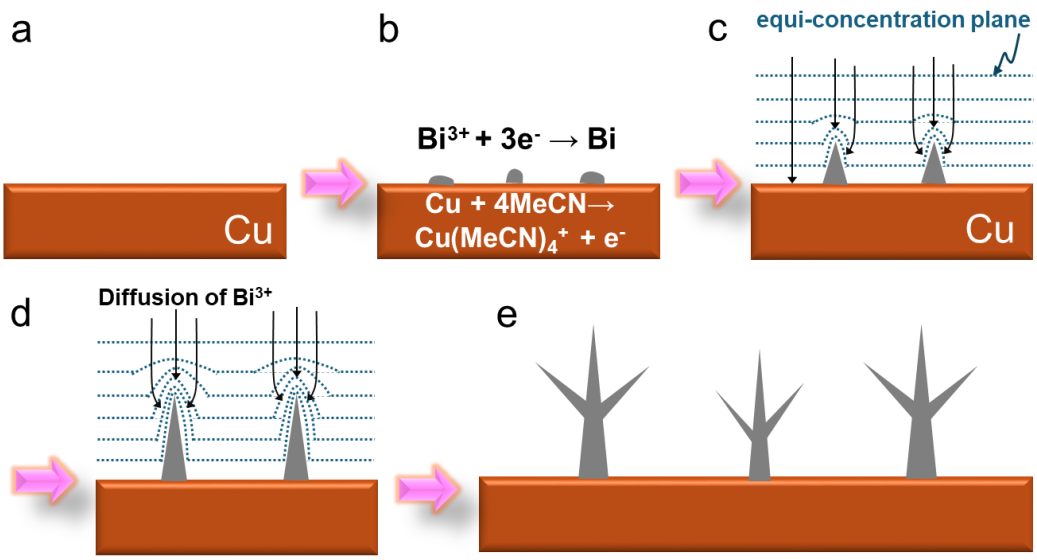

Fig. S4 The growth mechanism of Bi MF on porous Cu foil.

Based on the previous studies on the formation mechanism of metallic dendritic structures,[2-5] we proposed a possible growth mechanism of Bi MF on Cu foil:

The Bi MF were synthesized via galvanic replacement reaction[6, 7]: Bi^{3+} + 3Cu(s) + 12MeCN → Bi(s) + $3Cu(MeCN)_4^+$. When the porous copper foil being immersing in a bismuth salt aqueous solution containing acetonitrile, Bi^{3+} are reduced to Bi atoms at the surface of copper foil via an electron transfer from Cu metal due to the much higher standard electrode potentials of Bi^{3+}/Bi (0.308 V) than $Cu(MeCN)_4^+$/Cu (-0.048 V). At the initial stage, Bi atoms aggregate on the Cu surface to form an amorphous protuberance, which crystallize into a seed of Bi crystal. Due to the fast reaction rate of the Galvanic displacement reaction between Bi^{3+} and Cu, the concentration of Bi^{3+} near the growing fronts of crystals becomes very low, which greatly affects the mass transfer of Bi^{3+} (diffusion-limited conditions), leading to significant concentration polarization. At this stage, spherical diffusion layers for Bi^{3+} are formed in the electrolyte near the protrusions on the substrate, presenting a steeper concentration gradient compared to the electrolyte near flat areas. This steep gradient accelerates the diffusion of Bi^{3+} towards the Bi protrusions, which consequently promotes their rapid growth. The sharp crystal growth is generally accompanied by frequent branching in directions that are crystallographically equivalent, resulting in the formation of Bi dendrites (Bi MF).

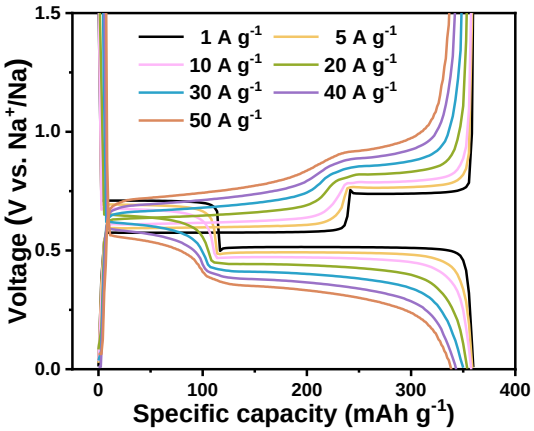

Fig. S5 GCD curves of Bi MF electrode at different current densities.

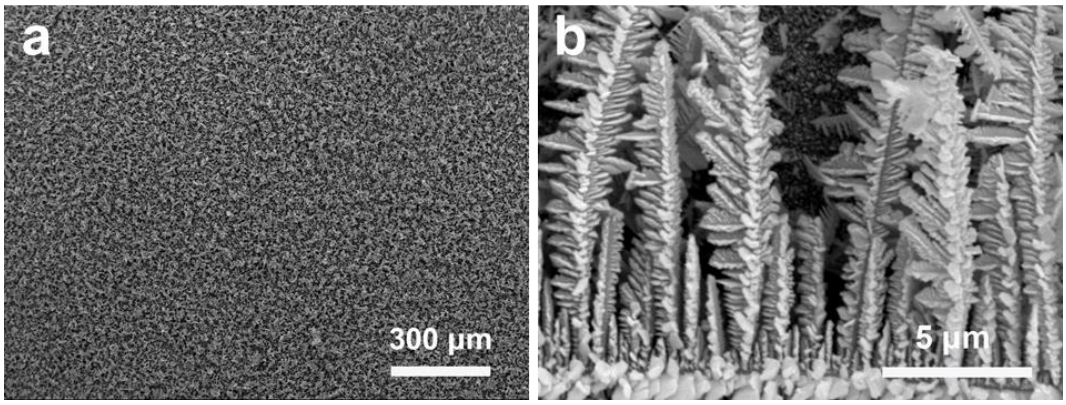

Fig. S6 SEM images of Bi MF on non-porous copper foil.

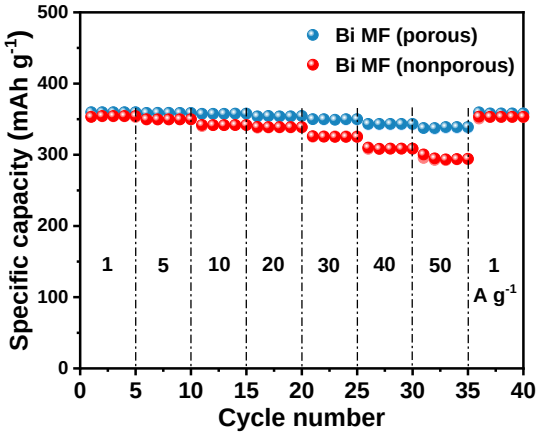

Fig. S7 Comparison of rate capability of the Bi MF on porous and non-porous copper foils.

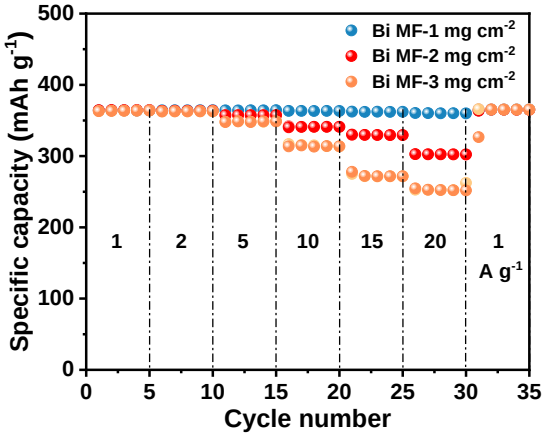

Fig. S8 Comparison of rate capability of the Bi MF at different mass loading.

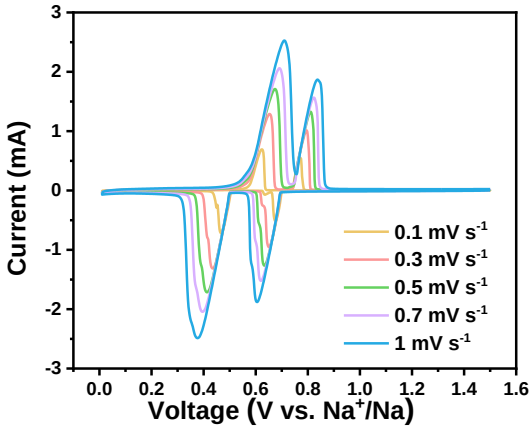

Fig. S9 CV curves of the bulk Bi at varying scan rates.

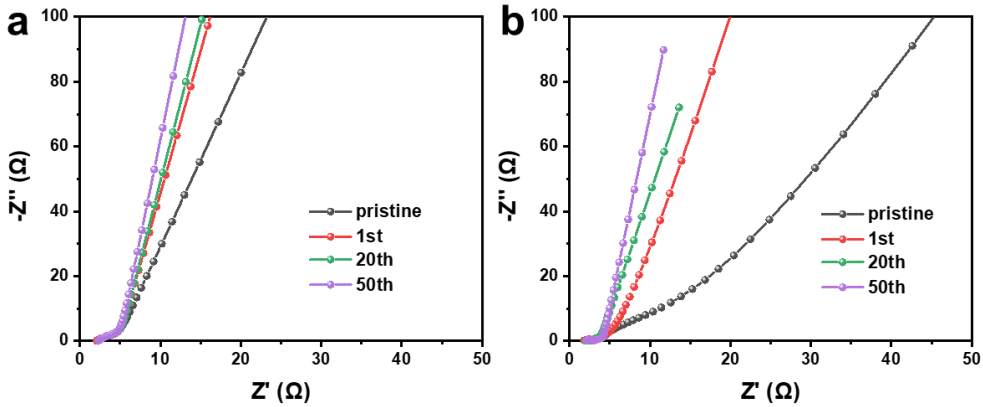

Fig. S10 Nyquist plots of (a) Bi MF, (b) bulk Bi after different cycles.

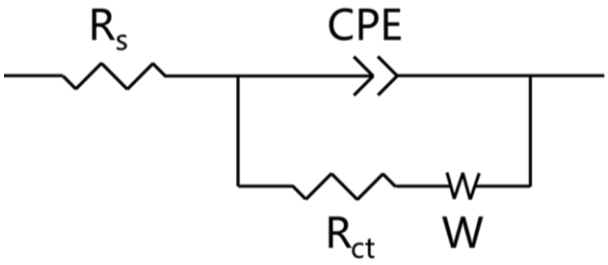

Fig. S11 The equivalent circuit model used for EIS fitting.

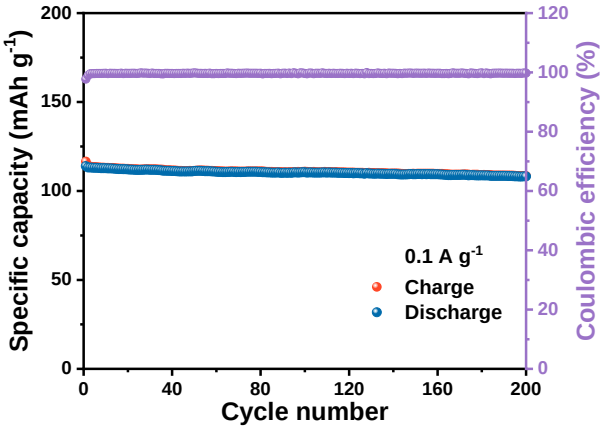

Fig. S12 Cycling performance of NVP cathode at 0.1 A g^{-1}.

The NVP electrode delivers an initial discharge capacity of 116.6 mAh g^{-1} and maintains a capacity of 94.9 mAh g^{-1} after 200 cycles.

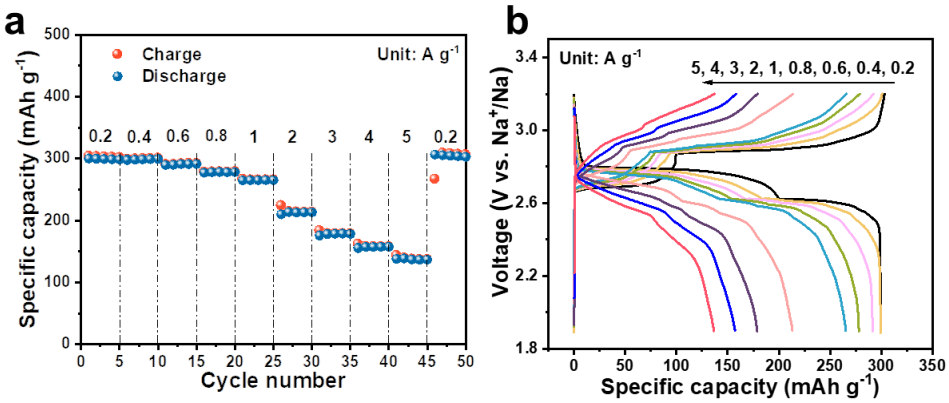

Fig. S13 (a) Rate capability, (b) GCD curves at different current densities of NVP // Bi MF full cell.

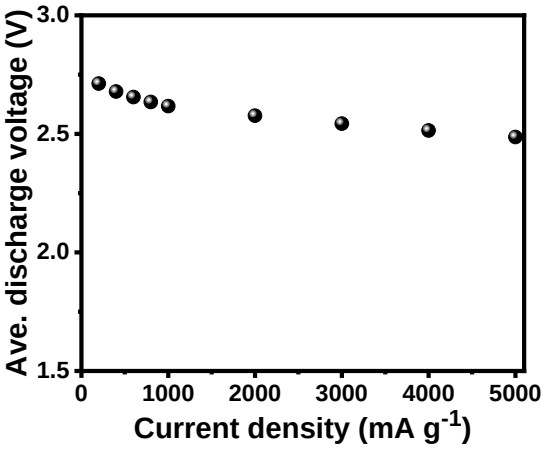

Fig. S14 The corresponding average discharge voltage at different rates of NVP // Bi MF full cell.

Table S1 Comparison of rate performance of Bi-based anodes for SIBs.

Sample	Current density ($A\ g^{-1}$)	Capacity ($mAh\ g^{-1}$)	Retention rate (%, Compared with 1 $A\ g^{-1}$)	Ref.
Bi MF	**1**	**359.7**	**--**	**This work**
	5	**358.9**	**99.8**	
	10	**357.5**	**99.4**	
	20	**353.9**	**98.4**	
	30	**350.0**	**97.3**	
	40	**343.4**	**95.5**	
	50	**338.9**	**94.2**	
Bi@NC	5	344.1	95.7	8
	10	338.2	94.1	
Bi@viod@C	5	255	94.4	9
	10	246	91.1	
	20	231	85.6	
	50	190	70.4	
Bi/Ni	2	206.4	--	10
Bi@N-C	5	262	87.3	11
	10	252	84.0	
	20	240	80.0	
	50	211	70.3	
Bi@3DGFs	5	208	96.3	12
	10	202	93.5	
	20	194	89.8	
	50	180	83.3	
ML-Bi@NCS	5	361	96.8	13
	10	349	93.6	
	20	327	87.7	
	30	288	77.2	
Bi@C	5	319	99.4	14
	10	316	98.4	
	20	307	95.6	
	30	297	92.5	
	40	283	88.2	
	50	274	83.4	

$C_{PVP+C2H2}$/Bi/rGO	5	373	98.2	15
	10	359	94.5	
	20	322	84.7	
	30	277	72.9	
	50	188	49.5	
Bi@NC composite	5	349.3	98.4	16
	10	341.5	96.3	

Table S2 Fitting results of the Nyquist plots shown in Fig. S10a using the equivalent electrical circuit model in Fig. S11.

Cycles	R_s (Ω)	R_{ct} (Ω)
Pristine	2.13	0.60
1st	2.10	0.48
20th	2.26	0.26
50th	2.22	0.05

Table S3 Fitting results of the Nyquist plots shown in Fig. S10b using the equivalent electrical circuit model in Fig. 11.

Cycles	R_s (Ω)	R_{ct} (Ω)
Pristine	2.67	0.82
1st	1.92	0.79
20th	1.93	0.46
50th	2.02	0.93

References

1. X. Li, S. Xiao, X. Niu, J. S. Chen and Y. Yu, *Adv. Funct. Mater.*, 2021, **31**, 2104798.

2. T. A. Witten and L. M. Sander, *Phys. Rev. Lett*., 1981, **47**, 1400-1403.

3. K. Fukami, S. Nakanishi, H. Yamasaki, T. Tada, K. Sonoda , N. Kamikawa, N. Tsuji, H. Sakaguchi and Y. Nakato, *J. Phys. Chem. C*, 2007, **111**, 1150-1160.

4. J. Chen, J. J. Davies, A. S. Goodfellow, S. M. D. Hall, H. G. Lancaster, X. Liu, C. J. Rhodes and W. Zhou, *Prog. Nat. Sci*., 2021, **31**, 141-151.

5. S. Xie, X. Zhang, D. Xiao, M. C. Paau, J. Huang and M. M. F. Choi, *J. Phys. Chem. C*, 2011, 115, 9943-9951.

6. X. Zhang, X. Sun, S.-X. Guo, A. M. Bond and J. Zhang, *Energy Environ. Sci.*, 2019, **12**, 1334-1340.

7. C. Zhu, Q. Wang and C, *J. CO_2 Util.*, 2020, **36**, 96-104.

8. L. Chen, X. He, H. Chen, S. Huang and M. Wei, *J. Mater. Chem. A*, 2021, **9**, 22048-22055.

9. H. Yang, L. W. Chen, F. X. He, J. Q. Zhang, Y. Z. Feng, L. K. Zhao, B. Wang, L. X. He, Q. B. Zhang and Y. Yu, *Nano Lett.*, 2020, **20**, 758-767.

10. L. B. Wang, C. C. Wang, F. J. Li, F. Y. Cheng and J. Chen, *Chem. Commun.*, 2018, **54**, 38-41.

11. H. Yang, R. Xu, Y. Yao, S. Ye, X. Zhou and Y. Yu, *Adv. Funct. Mater.*, 2019, **29**, 1809195.

12. X. L. Cheng, D. J. Li, Y. Wu, R. Xu and Y. Yu, *J. Mater. Chem. A*, 2019, **7**, 4913-4921.

13. X. X. Wang, Y. Wu, P. Huang, P. Chen, Z. Y. Wang, X. W. Xu, J. Xie, J. Yan, S. G. Li, J. Tu and Y. L. Ding, *Nanoscale*, 2020, **12**, 23682-23693.

14. Z. Li, W. Zhong, D. Cheng and H. Zhang, *J. Mater. Sci.*, 2021, **56**, 11000-11010.

15. C. J. Hu, Y. S. Zhu, G. Y. Ma, F. Tian, Y. L. Zhou, J. Yang and Y. T. Qian, *Electrochim. Acta*, 2021, **365**, 137379.

16. S. Wei, W. Li, Z. Ma, X. Deng, Y. Li and X. Wang, *Small*, 2023, **19**, 2304265.